Astronomy & Astrophysics manuscript no. wlflares
February 28, 2023

An Overview of HMI Off-Disk Flare Observations

D. Fremstad[1], J. C. Guevara Gómez[1,2], H. Hudson[3,4], and J. C. Martínez Oliveros[4]

[1] Institute of Theoretical Astrophysics, University of Oslo, Postboks 1029 Blindern, 0315 Oslo, Norway
[2] Rosseland Centre for Solar Physics, University of Oslo, Postboks 1029 Blindern, 0315 Oslo, Norway
[3] SUPA School of Physics and Astronomy, University of Glasgow, G12 8QQ, UK
[4] SSL, University of California, Berkeley CA 92037, USA
e-mail: j.c.g.gomez@astro.uio.no

Received December 24, 2022; accepted for publication

ABSTRACT

Context: White-light continuum observations of solar flares often have coronal counterparts, including the classical "white-light prominence" (WLP) phenomenon. **Aims:** Coronal emissions by flares, seen in white-light continuum, have only rarely been reported previously. We seek to use modern data to understand the morphology of WLP events. **Methods:** We have identified a set of 14 examples of WLP detected by the HMI (Heliospheric and Magnetic Imager) experiment on board SDO (the Solar Dynamics Observatory satellite), using a new on-line catalogue covering 2011-2017. These invariably accompanied white-light flares (WLF) emission from the lower atmosphere by flares near the limb, as identified by hard X-ray images from RHESSI (the Reuven Ramaty High Energy Spectroscopic Imager). HMI provides full Stokes information, and we have used the linear polarisations (Q and U) to distinguish Thomson scattering from cool material, following the analysis pioneered by Saint-Hilaire et al. (2014). **Results:** The event morphologies fit roughly into three categories: Ejection, Loop, and Spike, but many events show multiple phenomena. **Conclusions:** The coronal white-light continuum, observed by HMI analogously to the observations made by a coronagraph, detects many examples of coronal emission and dynamics. Using the Stokes linear polarisation, we estimate the masses of hot coronal plasma in 11 of the 14 events and find them to be similar to typical CME masses, but not exceeding 10^{15} g. We note that the HMI observations do not occult the bright solar disk and were not designed for coronal observations, resulting in relatively low signal-to-noise ratios. We therefore believe that future such observations with better optimisation will be even more fruitful.

Key words. Sun: Flares – Sun: filaments, prominences – Sun: corona – Sun: coronal mass ejections (CMEs)

1. Introduction

The Heliospheric and Magnetic Imager (HMI) has provided a large volume of solar observations at visible wavelengths in a narrow band including the photospheric Fe I line at 6173.34 Å (Scherrer et al. 2012; Hoeksema et al. 2014). These observations include a glimpse of the continuum near this wavelength and have sufficient time resolution to have captured many solar flares. The observations began 21 April 2010 and continue to the present, thus including the full sunspot maximum of Solar Cycle 24. HMI observes solar flares only because it patiently records the full Sun, with a very high duty cycle thanks to the geosynchronous orbit of the Solar Dynamics Observatory (Pesnell et al. 2012). Because HMI's principal scientific objectives are in helioseismology and in solar magnetism, its flare observations are serendipitous and not optimal for the purpose; nevertheless HMI has produced a unique record of the many events that comprise the survey reported here.

In another serendipitous bonus, HMI images extend into an annular region outside the solar disk, and Martínez Oliveros et al. (2014) noted that two X-class solar flares (SOL2013-05-13T02[1] and SOL2013-05-13T16) were detectable both on the disk (akin to classical white-light flares; see *e.g.* Neidig 1989; Hudson 2016), but also *above the limb*, providing a first systematic database for studying "white-light prominences", a extremely rare phenomena prior to HMI. Using HMI's full Stokes capability, Saint-Hilaire et al. (2014) found linear polarisation in some of these ejecta, making it possible to use the familiar tool of Thomson scattering to explore the flare corona right down to the limb of the Sun. HMI can thus detect two classes of flare events, which we refer to as on-disk (analogous to white-light flares) and off-disk (the white-light prominences). These often go together, especially for events near the limb. The off-limb component appears in the annular zone (the "annulus"), some tens of arcsec wide, just above the visible limb. HMI detects both of them in narrow-band "pseudocontinuum" (Švanda et al. 2018). This paper introduces a catalogue of HMI flare observations, kept online at the RHESSI/HMI White light Flare Catalogue [2]. We also review the morphology of the events, which have some novel features. To our knowledge, there is no other systematic catalogue of HMI off-disk events, but note that Namekata et al. (2017) reported a large survey of on-disk events as part of research on analogous stellar flares.

2. The Catalogue

Most white-light flare (WLF) observations have come from broad-band sensors, or (rarely) spectroscopic data. The HMI

[1] We name the events following the IAU target convention SOLyyyy-mm-ddThh:mm:ss

[2] http://sprg.ssl.berkeley.edu/~oliveros/wlf_catalogue/catalog.html

database we use differs substantially from either of these approaches: the "Ic" pseudo-continuum data product measures the continuum background for a photospheric absorption line over a narrow spectral band, using six wavelength samples over a tuneable range of 678 mÅ at the 6173.3 Å line (Hoeksema et al. 2014). This limited sampling has some disadvantages; it is a narrow slice of the continuum adjacent to a spectral line that wobbles in wavelength owing to the spacecraft Doppler motion, for example. In sunspot regions, where WLFs usually happen, the continuum level may be much less than that of the quiet photosphere. The line itself actually may go into emission during the flare. In spite of these caveats the flare observations do correlate well with independent observations as regards image morphology and time variations, with some uncertainties as regard absolute photometry (e.g. Švanda et al. 2018).

The Catalogue (at time of writing) listed 461 entries for M- and X-class flares in Cycle 24 and based on the RHESSI flare list for the years 2011 through 2016. Each entry contains intensity, running-difference and power intensity movies for flares within 70 degrees from disk centre and intensity, plus running-difference and saturated running-difference movies for limb and off-limb events. A linked script then returns a cutout HMI data cube for any selected event. See the Catalogue entry[3] for first off-limb detection, SOL2013-05-13T16:00 (X2.8), as reported by Martínez Oliveros et al. (2014). This remarkable event is one of the best detection in the HMI annulus, but the Catalogue contains many more examples as surveyed below in Section 3.

Difference imaging is the essential tool underlying most of the HMI flare observations. WLF events on disk are sometimes bright enough to be seen without this advantage (famously Carrington 1859; Hodgson 1859). In the annular region outside the disk, though, recognition is a little bit harder. This region is dominated by scattered light originating in the HMI optics, and the noise fluctuations of this unwanted signal dictate the sensitivity limit for flare observations. The annulus initially was limited to about 20″ in width, owing to SDO telemetry limitations, but was increased substantially after the 2013 observations showing the interesting things that could be seen there. Compare the examples in Figure 1 to see this improvement; it roughly doubled the width of the annulus to about 40″.

3. Morphologies of Off-limb White-Light flares

Using the Catalogue we are able to explore the coronal morphology of the white-light flares systematically. This is done by looking for flares with visible mass ejection in the HMI annulus region, where the detection sensitivity is much higher than on the disk because it has no direct photospheric signal. In this paper we have manually picked out 13 events from the Catalogue in which we can clearly observe activity above the limb. And we have included as well the SOL2017-09-10T flare for a total of 14 events. The continuum in general has several possible contributions (Hiei et al. 1992; Jejčič et al. 2018) and, because of the novelty of this database, we make no assumptions about the physical nature of the phenomena, instead proceeding initially just from morphological appearance. Candidate physical phenomena would include surges, sprays, jets, filament eruptions, CMEs, and flare-induced coronal "evaporation," for example.

We make rough morphological classifications of the flares by looking at the difference in intensity over time for each flare and observe the dynamics of the flare via movies and difference images, as contained in the Catalogue. We establish three tentative morphologies (see Sect. 3.5 and Fig. 3); Spikes, which appear as quick flashes of light close to the limb, Ejections (identified with loop prominence systems (LPS) in the classical Hα sense of Bruzek 1964), which appear as mass moving rapidly through the annulus and are observed to take place after Spikes, and Loops which are arc-shaped features appearing to move slowly outward from the limb. Some events exhibit multiple morphological properties, and typically the Spike component precedes the Loop component in time, mirroring the impulsive and gradual phases of flare development. Examples of these morphologies are shown in Figure 1, the images are shown as they come by default in HMI data, i.e., they are not rotated.

3.1. Analysis of On-Disk Flare Properties

With modern observations it is fairly common to observe some continuum emission from a flare (the WLF phenomenon), especially for the more energetic cases but also sometimes for minor events (Jess et al. 2008). In HMI movies such a flare appears as a quick flash of light on the disk, resolved upon inspection often to display two-ribbon or kernel structure (e.g., Hudson et al. 2006), often including diffuse brightening. Disk events not sufficiently close to the limb cannot be linked to the morphology of the off-disk event, unfortunately. The Catalogue includes the helioprojective position of the flare, its size, and the time, using the RHESSI onset time for the time field. It includes animations of the full data and of difference images, selecting the image frame in which the flare is clearly visible. From there we restrict the region and what intensities we include. For classification we fit an asymmetric 2D Gaussian kernel to it which gives us the position, length and width of the flare brightening:

$$I = I_0 e^{-\left(a(x-x_0)^2+2b(x-x_0)(y-y_0)+c(y-y_0)^2\right)} \quad (1)$$

where

$$a = \frac{\cos^2\theta}{2\sigma_x^2} + \frac{\sin^2\theta}{2\sigma_y^2} b = -\frac{\sin 2\theta}{4\sigma_x^2} + \frac{\sin 2\theta}{4\sigma_y^2} c = \frac{\sin^2\theta}{2\sigma_x^2} + \frac{\cos^2\theta}{2\sigma_y^2}, \quad (2)$$

thus making six free parameters (the helioprojective position $[x, y]$, the length and width $[\sigma_x, \sigma_y]$, the peak intensity I_0 and the rotation angle θ). This process is done manually; an example appears in Figure 2. In this case the proximity to the limb of the on-disk emission results in a highly elongated 2D Gaussian fit. Table 1 summarises the kernel parameters for the on-disk events in the Catalogue.

3.2. Analysis of Off-limb Flare Properties

The dynamics seen in the off-limb observations is a key part of the morphological description. We quantify this by creating time-distance plots which give visual timelines of the flare dynamics and can be further used to estimate the plane-of-the-sky velocity of the ejected mass. These plots show the evolution of ejected mass in height over time and allow us more easily see the dynamics of the ejected mass and thus gives us a better understanding of the flares morphology. There are several steps that goes into making a plot that clearly displays the dynamics of the flare. We begin by cropping out the solar disk and rotating the frame such that the solar limb is horizontal. We select a central pixel, which preferably is centred on the main body of the ejected mass. Next we select some distance, d, from the central

[3] Event No. 14 at https://sites.google.com/berkeley.edu/hsi-hmi-catalog/2013

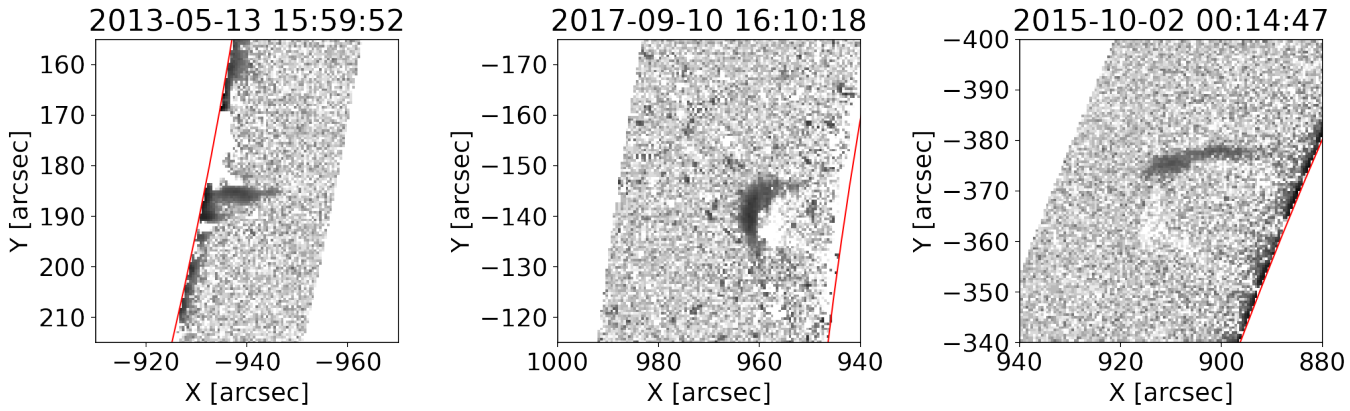

Fig. 1. Example of the Spike (left; SOL2013-05-13T01:50), Ejection (middle; SOL2017-09-10T) and Loop (right; SOL2015-10-02T00:07) coronal flare morphologies. Date and time of each snapshot is listed above each figure. Note the increase of annulus width between 2013 and 2015. These are running difference images, from the 45-s cadence of the original data, with black showing newly appearing emission.

Table 1. On-disk flare kernel parameters. The first column is the start time of the flare as listed in the RHESSI catalogue. The second column is the time of the WL-brightening. The third and fourth columns give the helioprojective x and y coordinates in arcseconds. The fifth and sixth columns describe the standard deviations of the Gaussian kernel along its major (σ_2) and the minor axes (σ_1). The seventh column shows the centre averaged raw intensity of the flare with respect to the average intensity of the solar disk centre. While the last column shows the rotation angle of the Gaussian kernel with respect to the vertical axis, i.e., the clockwise rotation of the kernel with respect to north-south in degrees.

Event (RHESSI Start Time)	t_{WL}	x_0	y_0	σ_1	σ_2	$I_0/I_\odot$	θ
SOL2011-01-28T00:46	00:57	936	277	0.2	0.5	0.11	-19
SOL2011-09-22T10:53	10:52	-921	159	0.4	0.5	0.35	0
SOL2011-10-31T17:48	17:47	-937	204	0.2	0.5	0.51	-2
SOL2012-03-02T17:54	18:40	-914	305	0.5	0.9	0.41	34
SOL2012-11-08T02:06	02:19	-926	233	0.5	1.2	0.55	55
SOL2012-11-20T12:28	12:39	952	198	0.3	2.5	0.17	-14
SOL2013-05-13T01:50	02:08	-930	192	0.3	9	0.12	11
SOL2013-05-13T15:50	15:59	-931	181	1.2	6.3	0.32	16
SOL2014-10-16T12:58	13:01	-937	-221	0.4	4.5	0.19	-12
SOL2014-11-03T22:08	22:31	-936	244	0.4	9.8	0.24	14
SOL2015-03-02T15:15	15:24	899	360	0.2	8	0.19	-20
SOL2015-10-02T00:08	00:10	819	-364	1.7	3.3	0.60	-2
SOL2015-10-02T12:21	12:30	883	-330	0.3	0.9	0.61	16
SOL2017-09-10T16:05	15:58	942	-153	0.5	0.7	0.2	2

pixel and calculate the mean intensity from pixels with distance less than d from the central pixel. This is done for each height in the frame and leaves us with a strip of mean intensities for different heights. We subtract the continuum intensity from this at each height, which is found by calculating the mean intensity at each height for some time before or after the mass ejection takes place and then taking the mean of these intensities. We are thus left with a slice of corrected mean continuum excess intensity. Doing this for each frame, leaves us with results such as that shown in bottom panel of Figure 4. We can clearly see how the height of the ejected mass evolves over time, giving a clear view of the time evolution of the coronal aspects of the flare in the manner that a coronagraphic J-map does (Sheeley et al. 1999).

We calculate speeds for each ejection event by fitting a Gaussian to the signal at each height. The mean of the Gaussian thus traces the flare in time. Figure 4 shows an example of such a trace. The mean at each height can then be fitted with a linear function where the slope gives us the velocity projected in the plane of the sky. The flare emission has substantial noise fluctuations, resulting in gaps where the Gaussian fits do not converge. As an example in Figure 4 we would use the column of points at the bottom to find the velocity of the first part of the flare, the Spike, and the curve at the top for the second part, the Loop, but the points in between them are not relevant and should be ignored. We thus make two separate linear fits for the two parts.

3.3. Emission Mechanisms

Hiei et al. (1992) described the mechanisms likely to produce the emissions detected with HMI: Thomson scattering, recombination radiation (free-free and free-bound), and line emission.

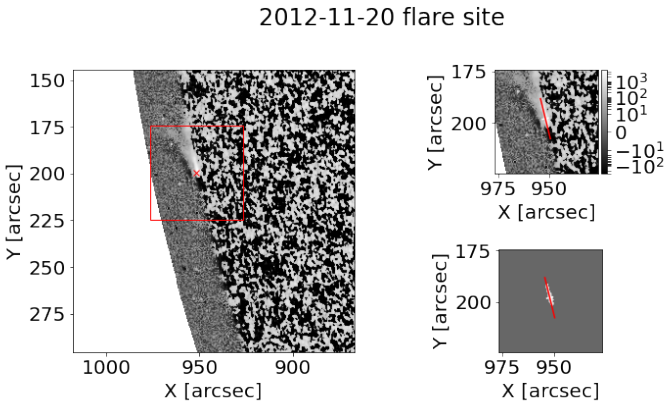

Fig. 2. Flare site and kernel fit for SOL2012-11-20T12:27, an ejective event. This is again a running-difference frame with new emission shown in white.

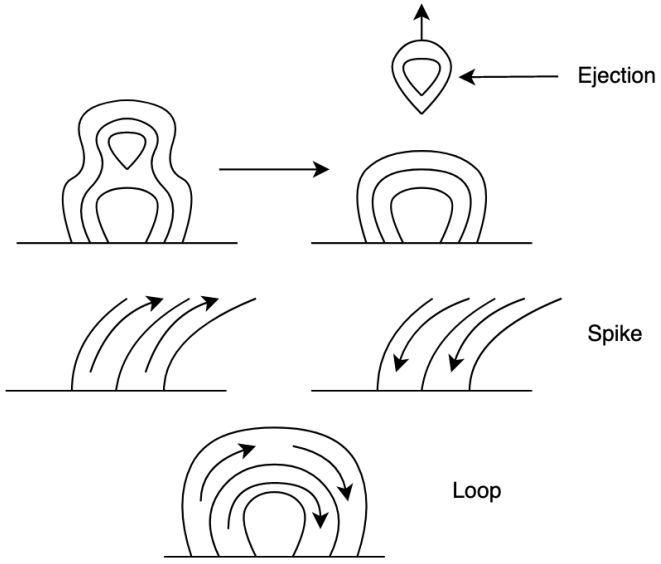

Fig. 3. Illustration of the three morphologies. For the LPS or ejection, we see that it is the magnetic field lines itself that form an independent loop and travels away from the limb. For the Spike and Loop morphology, the ejected mass follows the magnetic field lines. In the case of the Loop, the ejected mass follows the magnetic field lines all the way around the loop, while for the Spike we only observe them to follow it partially.

The latter mechanisms (atomic processes) need not be optically thin if the source densities are large enough (Jejčič et al. 2018). HMI's capability for linear polarisation makes detection of the Thomson-scattering component unambiguous, within signal-to-noise limitations. To disentangle the atomic processes requires consideration of radiative transfer and source geometry. Martínez Oliveros et al. (2014) included detection of the HMI target line (6173 Å), normally an absorption line in the quiet Sun, to appear in emission in the legs of the Ejection event SOL2013-05-13T16:01 (their Fig. 1). Generally we can imagine such sources to be optically-thick extensions of the photosphere itself, and thus to have the potential to be much brighter than the Thomson-scattered sources.

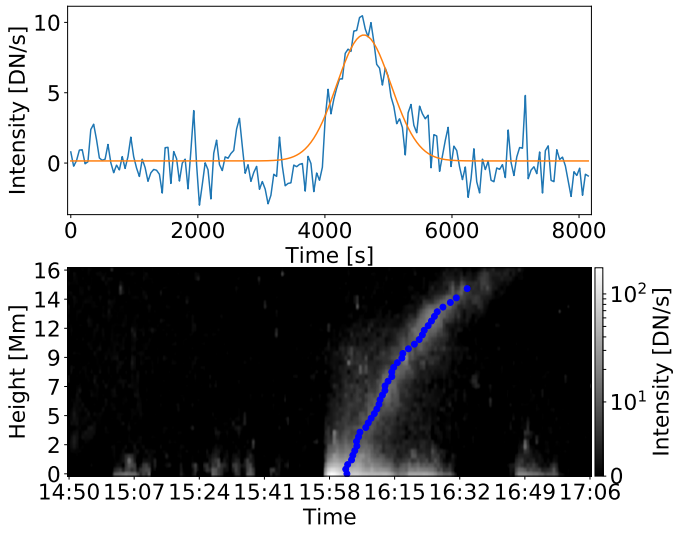

Fig. 4. Gaussian fit for flare SOL2013-05-13T15 (middle panel in figure 1). The top panel shows the fit compared to the intensity for a horizontal slice in the middle of the time-distance plot and the bottom panel shows the trace given by the mean of the Gaussian fit at each height. We can see traces of the Spike morphology as an illumination at the bottom of the figure, in addition to the Ejection (LPS) morphology which again is seen as a cloud appearing after the Spike.

3.4. Masses

We are also able to estimate the events masses and column densities by assuming Thomson scattering as the dominant mechanism. This is the same as the usual analysis of the K-corona (Billings 1966), with the advantage that we can assume a localised source, rather than a spherically extended 3D corona. We discuss this assumption further below. The method for calculating these quantities is described in Martínez Oliveros et al. (2022), where the mass and column density of the SOL2017-09-10 off-limb flare was measured to be in the order of $8 \cdot 10^{14}$ grams and 10^{21} cm^{-2} respectively.

This method requires estimates of the linearly polarised flux, which HMI provides at a 12 min cadence. The Q and U polarisation components are rotated into the frame of the solar limb, such that the rotated Q' component contains all of the linear polarisation for a simple photospheric radiation field (see Saint-Hilaire et al. 2021). We define a region of interest around the Stokes I source and integrate the Q' signal in a preflare-subtracted difference image. For some of the events, especially those of Spike morphology, the mass could not be calculated well, owing to the complex and noisy image configuration and its proximity to the limb. We obtain such an estimate for each frame to create a time series.

The mass estimates based on the polarisation reflect only the Thomson scattering, and on this basis may underestimate the total masses of the events.This is because any cool component may not be fully ionised. We can safely assume that the Thomson component is optically thin, so unless a part of the source is occult by foreground material the mass estimate should closely match the amount of material injected at high temperatures into the flare loops (e.g. Hudson & Ohki 1972). The mass estimation for the Spike morphology in particular, or any cool material, would depend upon detailed radiative-transfer modelling that we have not attempted in this article.

3.5. Morphologies

As previously mentioned there are three morphologies found in this study; Spike, Ejection, and Loop. With the methods described above we have made time-distance plots and estimated the projected velocities for each of these. Roughly speaking, Spike events seem similar to surges and sprays, Ejection events to the loop prominences, and Loop events to flows confined to closed coronal fields. The examples we discuss below show surprises, though, and we cannot be sure that our three morphologies capture all of the possibilities.

The Spike morphology is defined by rapid motion, somewhere between 100 km/s and 300 km/s. In view of this, the low cadence of HMI image sequences make polarisation measurements extremely uncertain. In general, the loss of polarisation data in this way tends to make our mass estimates lower limits. Spikes can appear as columns of mass ejected away from the solar disk or as large bursts that seemingly do not escape far from the disk and happen very quickly. In addition to this they do not reach very large heights. We find instances where the ejected mass during Spikes move away from the limb but also at least one with rapid motions towards the limb, which we would identify with coronal rain. The natural explanation for outward-moving Spike events would be as the HMI counterpart of the common Hα surge or spray. An illustration of the Spike morphology is shown in the middle drawings in Figure 3 and an example of a Spike time-distance plot can be found in the bottom panel of Figure 4. Martínez Oliveros et al. (2014) also reported Spike-like behaviour but with *downward* motion in SOL2012-05-13 (see below for further comments). This velocity, plus the appearance of bright material from the corona, strongly suggests an identification with the late phase of coronal rain.

The Ejection morphology appears only to happen after a Spike event. It is apparent that the Spikes initiates the loop prominence systems and might give rise to the ejected mass that goes into making a loop prominence system. The Ejection morphology in HMI appears as long clumps of gas that are spread out over a larger period of time in the time-distance plot. The small velocity of this morphology causes it to have a very distinct fingerprint on the time-distance plots. In Table 2 we can see that the velocities of LPS are usually of order of magnitude $\sim$ 10 km/s, which is consistent with what is found in Hα by Bruzek (1964). In this case the magnetic field forms independent loops that appear to carry the mass away from the limb, as illustrated by the top drawing in figure 3.

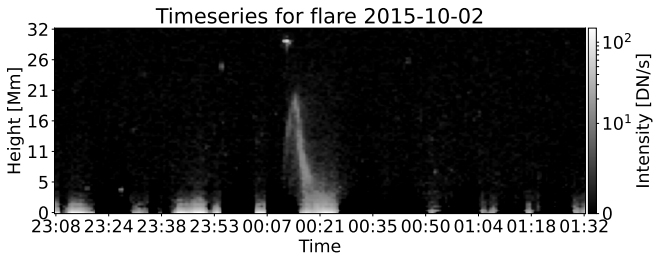

Fig. 5. Time series for the SOL2015-10-02 CME showing Loop morphology.

The Loop morphology appear to reflect parallel flow within loops. Instead of a Spike ejecting mass that may eventually form into an LPS, the ejected mass follows an isolated, stationary arch, ascending in one branch and descending in the other (Bruzek 1964). Such behaviour suggests the participation of cool material. See the bottom drawing in figure 3 for an illustration of the Loop morphology. In the time-distance plot the Loop morphology appears as two long columns connected at the top. We can measure the upwards and downwards velocity of the loop by restricting which part of the time-distance plot we want to fit a Gaussian to. If we cut the plot along the middle of the loop we can fit a Gaussian and then a linear function to the left side of the loop which gives us the upwards moving velocity, while the right side gives us the velocity moving down. The Loops differ from the similar Ejection (loop prominence systems) because they show apparently parallel flow, do not travel to larger heights and have higher velocities.

The complete evolution in height over time for each flare as a result of tracing the flares by fitting a Gaussian to each height is plotted in figure 6. We find that for all cases of LPS the ejected mass is always propagating away from the Sun. Similar results to what is shown in the left panel is also reported by Bruzek (1964). In the case of the Spikes we can also find cases where the mass is moving away from the Sun, but we also find evidence that they can fall down back onto the Sun. In addition, the SOL2015-10-02 event shows evidence of Loop morphology can be seen to move away from the Sun before reversing.

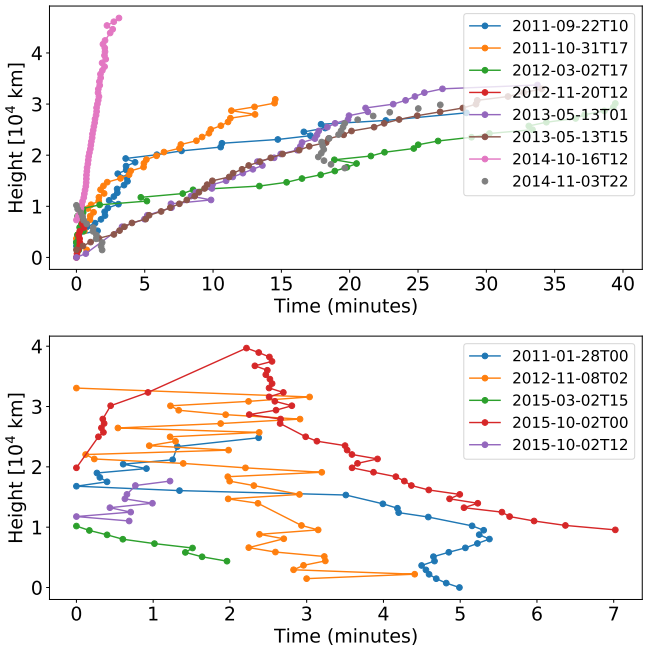

Fig. 6. Resulting time evolution in height for the included flares from tracing the flares using a Gaussian fit for each height. The flares that are found to be propagating away from the Sun are plotted in the top panel, while those that appear to fall back onto the sun are plotted in the bottom panel.

Summarising the appearance and behaviour of the HMI off-limb observations, we suggest that the Spike morphology corresponds to flare surge/spray activity during the impulsive phase, and that Ejection may correspond to filament eruptions. The Ejection morphology is well understood from the classic behaviour of the Hα loop prominence systems. A possible fourth morphology, Rain, may be present. This would describe the infall observed by Martínez Oliveros et al. (2014) in the event SOL2013-05-15T16:01 in which material appeared suddenly within the annular region and moved downward at a projected speed estimated at 134±8 km/s; the act of appearance strongly

Event	Spike velocity [km/s]	LPS velocity [km/s]	Loop velocity [km/s]	$N_e[cm^{-2}]$	$m[g]$	$\Delta Q'/\Delta I$	$I_0/I_\odot$
SOL2011-01-28T00:46	-47 ± 20	–	–	$3 \cdot 10^{20}$	10^{14}	0.07	$8.1 \cdot 10^{-3}$
SOL2011-09-22T10:53	61 ± 35	7 ± 8	–	$5 \cdot 10^{20}$	$3 \cdot 10^{14}$	0.11	$8.6 \cdot 10^{-3}$
SOL2011-10-31T17:47	–	30 ± 19	–	$4 \cdot 10^{20}$	$2 \cdot 10^{14}$	0.02	$9.0 \cdot 10^{-3}$
SOL2012-03-02T17:54	124 ± 34	9 ± 5	–	–	–	–	–
SOL2012-11-08T02:06	-102 ± 16	–	–	–	–	–	–
SOL2012-11-20T12:28	209 ± 39	–	–	–	–	–	–
SOL2013-05-13T01:50	-	18 ± 10	–	$5 \cdot 10^{20}$	$3 \cdot 10^{14}$	0.02	$5.5 \cdot 10^{-3}$
SOL2013-05-13T15:50	-	15 ± 5	–	$6 \cdot 10^{20}$	$3 \cdot 10^{14}$	0.02	$6.8 \cdot 10^{-3}$
SOL2014-10-16T12:58	270 ± 31 -72 ± 26	–	–	$5 \cdot 10^{20}$	$3 \cdot 10^{14}$	0.02	$6.8 \cdot 10^{-3}$
SOL2014-11-03T22:08	-64 ± 11	13 ± 10	–	$2 \cdot 10^{20}$	$9 \cdot 10^{13}$	0.02	$6.3 \cdot 10^{-3}$
SOL2015-03-02T15:15	-46 ± 11	–	–	$3 \cdot 10^{20}$	$2 \cdot 10^{14}$	0.10	$6.9 \cdot 10^{-3}$
SOL2015-10-02T00:08	217 ± 37	–	-87 ± 25	$2 \cdot 10^{20}$	10^{14}	0.06	$7.8 \cdot 10^{-3}$
SOL2015-10-02T12:21	–	69 ± 22	–	$2 \cdot 10^{20}$	10^{14}	0.09	$8.2 \cdot 10^{-3}$
SOL2017-09-10T16:05	33 ±12	11 ± 4	–	$2 \cdot 10^{21}$	$9 \cdot 10^{14}$	0.02	$7.3 \cdot 10^{-3}$

Table 2. Projected velocities of the respective morphologies. The first column shows the event time. The first second and third columns show the measured (projected) velocity for the morphology type present during that flare. The fifth and sixth column shows the inferred electron density and the total mass of the polarised component, based on peak polarisation signal and avoiding the Spike morphology as described in the text. The seventh column shows the measured polarisation and the eight column shows the normalised intensity of the ejected material. The large uncertainties in the measurements basically restrict the interpretation to one significant figure

.

suggests an identification with thermal instability (Field 1965) and the enhancement of HMI low-temperature opacity, rather than Thomson scattering by hot electrons. This observation required special analysis at HMI's highest time resolution, using all of the polarisation/wavelength images each differenced against its preceding like exposure. See Sun et al. (2017) for a discussion of high-cadence data from HMI. This kind of analysis was beyond the scope of the present paper, and so this event does not appear in the lower panel of Figure 6.

4. Conclusion

The pseudo-continuum observations of the Sun from HMI constitute a unique database for characterising solar white-light flares (WLF), and include the first-ever systematic view of WLF manifestations in the low corona from an observatory in space. These off-limb observations follow and extend a very limited historical set of data, mainly visual, of "white-light prominences". This paper introduces an on-line Catalogue[4] with comprehensive coverage of the off-limb events observed by HMI and further analysis of the on-disk morphology as well.

The catalogue reveals three distinct non-exclusive morphologies – Spike, Ejection, and Loop, which produce effect in an annulus about 40″ in width above the visible disk.

The full Stokes capability of HMI show that Thomson scattering plays a major role in WLF ejecta (Scherrer et al. 2012). This is the classic coronagraphic K-corona observational mode, extended to the base of the corona where the incident radiation field may have significant anisotropy (Saint-Hilaire et al. 2021). In some cases the off-limb structures achieve sufficient density (above about 10^{12} cm^{-3}) to allow normal collisional excitation to play a role (Jejčič et al. 2018). The linear polarisation, however, allows for a direct determination of the ejected mass (Martínez Oliveros et al. 2022).

[4] http://sprg.ssl.berkeley.edu/~oliveros/wlf_catalogue/catalog.html

Acknowledgments

J.C.G.G is supported by the SolarALMA project, which received funding from the European Research Council (ERC) under the European Union's Horizon 2020 research and innovation programme (grant agreement No. 682462), and by the Research Council of Norway through its Centres of Excellence scheme, project number 262622. H.H. thanks the School of Physics and Astronomy, University of Glasgow, for hospitality.
Data sources: All data used in this article can be found in public-domain archives.

References

Billings, D. E. 1966, A guide to the solar corona
Bruzek, A. 1964, ApJ, 140, 746
Carrington, R. C. 1859, MNRAS, 20, 13
Field, G. B. 1965, ApJ, 142, 531
Hiei, E., Nakagomi, Y., & Takuma, H. 1992, PASJ, 44, 55
Hodgson, R. 1859, MNRAS, 20, 15
Hoeksema, J. T., Liu, Y., Hayashi, K., et al. 2014, Sol. Phys., 289, 3483
Hudson, H. S. 2016, Sol. Phys., 291, 1273
Hudson, H. S. & Ohki, K. 1972, Sol. Phys., 23, 155
Hudson, H. S., Wolfson, C. J., & Metcalf, T. R. 2006, Sol. Phys., 234, 79
Jejčič, S., Kleint, L., & Heinzel, P. 2018, ApJ, 867, 134
Jess, D. B., Mathioudakis, M., Crockett, P. J., & Keenan, F. P. 2008, ApJ, 688, L119
Martínez Oliveros, J. C., Guevara Gómez, J. C., Saint-Hilaire, P., Hudson, H., & Krucker, S. 2022, ApJ, 936, 56
Martínez Oliveros, J.-C., Krucker, S., Hudson, H. S., et al. 2014, ApJ, 780, L28
Namekata, K., Sakaue, T., Watanabe, K., et al. 2017, ApJ, 851, 91
Neidig, D. F. 1989, Sol. Phys., 121, 261
Pesnell, W. D., Thompson, B. J., & Chamberlin, P. C. 2012, Sol. Phys., 275, 3
Saint-Hilaire, P., Martínez Oliveros, J. C., & Hudson, H. S. 2021, ApJ, 923, 276
Saint-Hilaire, P., Schou, J., Martínez Oliveros, J.-C., et al. 2014, ApJ, 786, L19
Scherrer, P. H., Schou, J., Bush, R. I., et al. 2012, Sol. Phys., 275, 207
Sheeley, N. R., Walters, J. H., Wang, Y.-M., & Howard, R. A. 1999, J. Geophys. Res., 104, 24739
Sun, X., Hoeksema, J. T., Liu, Y., Kazachenko, M., & Chen, R. 2017, ApJ, 839, 67
Švanda, M., Jurčák, J., Kašparová, J., & Kleint, L. 2018, ApJ, 860, 144